Nanoscale

Accepted Manuscript

This article can be cited before page numbers have been issued, to do this please use: Y. Liu, D. Ji, S. Liu, X. Qi, C. Lin, H. Liu, Y. Ji, Y. Liu and W. Lu, *Nanoscale*, 2026, DOI: 10.1039/D5NR04935K.

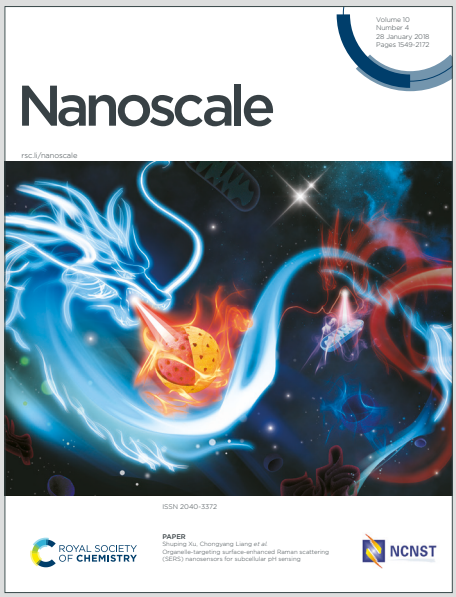

ROYAL SOCIETY OF CHEMISTRY

rsc.li/nanoscale

View Article Online
DOI: 10.1039/D5NR04935K

ARTICLE

Polydopamine-Coated Triamcinolone Acetonide Acetate Nanocrystals: Prevention of Postoperative Peritoneal Adhesion by Combining Anti-inflammation, Oxidative Stress Scavenging and Cytokine Adsorption

Received 00th January 20xx,
Accepted 00th January 20xx

DOI: 10.1039/x0xx00000x

Yaodong Liu[a], Daiheng Ji[a], Sixuan Liu[b],Xiaoxue Qi[a], Chenyi Lin[a], Hui Liu[b], Yajie Ji[b],Yu Liu[a,c*], Weiyue Lu[a].

Prevention of postoperative abdominal adhesion (PA) remains inadequately addressed by current clinical practice due to difficulties in precise regulation of inflammation and elimination of peroxidation products. This study proposed a polydopamine-coated triamcinolone acetonide acetate nanocrystal (TAA@PDA) to prevent peritoneal adhesions via the collective effects of TAA and PDA through multiple mechanisms, including anti-inflammatory effect, oxidative stress (ROS/RNS) scavenging, certain hemostatic ability and adsorption of pro-inflammatory cytokine by numerous amino/phenolic hydroxyl groups. TAA@PDA particles with a rod-like morphology and an average diameter of approximately 560 nm were successfully prepared via ball milling. TAA@PDA demonstrated excellent physical stability for up to 30 days, ensuring complete drug release within 7 days without sedimentation or aggregation. Anti-inflammatory and anti-oxidative capabilities of TAA@PDA were proven by their strong adsorption with pro-inflammatory cytokines (e.g., IL-6 and TNF-α), low adsorption capacity of anti-inflammatory IL-10 and ~80% efficiency in scavenging reactive oxygen/nitrogen species (ROS/RNS). TAA@PDA's adsorption of type I collagen and strong tissue adhesion rate demonstrated its retention capacity on the abdominal wall or organ surfaces. At the cellular level, TAA@PDA inhibited intracellular production of ROS, and effectively suppressed secretion of the inflammatory marker nitric oxide (NO). TAA@PDA exhibited certain hemostatic ability for small wound bleeding in abdominal injury. TAA@PDA significantly inhibited abdominal adhesion formation in PA model animals with a low incidence of severe adhesion (9.1%) which was only 1/8 that of the commercial anti-PA hyaluronic acid gel and 1/5 that of uncoated TAA NC, further supported by excellent anti-inflammatory performance and significantly reduced collagen deposition shown by pathological examination. In conclusion, this TAA@PDA might provide an efficient solution to prevent postoperative peritoneal adhesion by precise coordination between inflammatory microenvironment regulation and tissue protection.

Introduction

Postoperative peritoneal adhesion (PA) is abnormal fibrous connections formed during healing of visceral or tissue trauma caused by surgery, representing the most common complication following abdominal or pelvic procedures.[1] Statistically, PA incidence reaches approximately 66% with gastrointestinal surgeries carying the highest risk and colon/rectum being the most risky organs within the first postoperative year.[2,3] Diverse factors contribute to adhesion formation, including trauma, infection, ischemia, foreign body reactions, and peritoneal dissection or suturing-induced tissue ischemia.[4,5] Pathologically, PA results from dysregulation of the tissue repair process, leading to adverse outcomes such as chronic abdominal pain, intestinal obstruction and female infertility. Severe PA cases even require surgical adhesiolysis, which is still related with high recurrence rates and possible further aggravate peritoneal damage, perhaps creating a "adhesion-surgery-readhesion" vicious cycle.[6,7]

PA involves complex interactions where hemorrhage, hypoxia, and local inflammation are pivotal in driving pathological fibrosis.[8] As a metabolically active organ, the peritoneum activates intricate immune-inflammatory cascades upon injury.[9,10] Both mesothelial cells and resident peritoneal immune cells secrete inflammatory mediators in response to endogenous or exogenous trauma. Excessive inflammation recruits massive immune cell infiltration to the injury site, inducing immunosuppression that accelerates PA progression.[11] Abdominal surgery further causes vascular damage and subsequent hypoxemic hypoxia, triggering intracellular stress responses including hypoxia-inducible factor activation, lactate accumulation, and overproduction of reactive oxygen/nitrogen species (ROS/RNS).[12] Elevated ROS/RNS coupled with impaired antioxidant defenses activate coagulation cascades and increase thrombin generation, which disrupts the fibrinolysis equilibrium and promotes pathological fibrin deposition.[13] Critically, ROS upregulates adhesion-related mediators—including tumor necrosis factor-α (TNF-α), interleukin-6 (IL-6), transforming growth factor-β1 (TGF-β1), α-smooth muscle actin (α-SMA), and vascular endothelial growth factor—that exacerbate inflammation and fibrotic scarring.[14] Consequently, effective strategies to scavenge surgical-site ROS and suppress inflammation are essential for improving PA prevention, as confirmed by recent nanoparticle-microgel systems that demonstrate dual ROS-scavenging and anti-inflammatory efficacy in preclinical models.[15]

Although minimally invasive surgery is regarded as the optimal strategy, ideal avoidance of peritoneal injury remains unattainable. Consequently, research on anti-adhesion agents and physical barriers has gained significant attention. Systemic administration of anti-inflammatory/anticoagulant agents (e.g., NSAIDs, dexamethasone, heparin) shows limited clinical efficacy in preventing peritoneal adhesions. The core bottleneck is unavoidable systemic adverse effects. Approved physical barriers like Interceed™ (oxidized regenerated cellulose) and Seprafilm™ (sodium hyaluronate and carboxymethyl cellulose) still face practical limitations in

[a.] Department of Pharmaceutics, School of Pharmaceutical Sciences, Fudan University, Shanghai, 201203 China. E-mail: 23211030018@m.fudan.edu.cn.
[b.] Shanghai Shuguang Hospital Affiliated with Shanghai University of Traditional Chinese Medicine, Department of Breast Surgery, 201203 China.
[c.] State Key Laboratory of Advanced Drug Formulations for Overcoming Delivery Barriers, Shanghai, 201203 China.

Supplementary Information available: [details of any supplementary information available should be included here]. See DOI: 10.1039/x0xx00000x

application and demonstrate sub-optimal anti-adhesion efficacy, with potential long-term safety concerns.[16,17]

Recent years have seen the development of bioactive and effective anti-adhesion materials. An activated carbon-reinforced superstructured porous hydrogel (SPVA-AC) was developed, where activated carbon enhances mechanical stability while scavenging ROS and inflammatory cytokines to remodel the immune microenvironment.[18] Sun et al. prepared an injectable hydrogel loaded with adipose-derived mesenchymal stem cell (ADSC)-derived exosomes (Exos). This material alleviated oxidative stress, regulated inflammatory responses, and promoted macrophage polarization through exosome-mediated intercellular communication, thereby preventing adhesion formation.[19] Biodegradable 'Janus' zwitterionic hydrogel patches also effectively prevented adhesions by achieving strong tissue adhesion through a unilateral polymer brush layer while retaining antifouling properties on the opposite side to prevent organ adhesion, thereby promoting tissue repair.[20] These advanced materials address the bioinertness issues of traditional physical barriers through structural modifications or the incorporation of bioactive components, thereby endowing them with unique properties and demonstrating promising efficacy. However, their complex structures, potential safety concerns, and high production costs have limited clinical translation. In contrast, our developed TAA@PDA features simple structure and convenient administration.

A clinical practice demonstrated that patients receiving intraperitoneal injection of 200 mg triamcinolone acetonide (TA) in 500 mL dextran had peritoneal adhesion incidence reduced from 71% to 32% after myomectomy.[21] The proposed mechanism involves significantly upregulating mitochondrial function to prevent ROS formation, inhibiting TGF-β1 release, and reducing irreversible transformation of peritoneal fibroblasts to an adhesive phenotype. Triamcinolone acetonide acetate (TAA), which enhances safety and local efficacy durability through acetyl group modification of TA, may be more suitable for preventing peritoneal adhesions, inspiring researchers to conduct more studies to optimize its clinical applicability.[22,23] Triamcinolone acetonide acetate nanocrystals (TAA NC) with a particle size of approximately 270 nm could be prepared via wet ball milling; however, they are prone to agglomeration, presenting significant stability issues. Concurrently, considering the oxidative stress and inflammatory characteristics of peritoneal adhesions, an appropriate coating material is required to modify these nanocrystals, aiming to enhance both their stability and their anti-inflammatory and antioxidant capabilities.

Polydopamine (PDA), a melanin-like biopolymer mimicking mussel adhesion proteins, achieves nanoparticle surface functionalization via metal chelation, hydrogen bonding and electrostatic interactions derived from its catechol/primary amine groups.[24,25] PDA also provides antioxidant activity by blocking radical generation, directly scavenging ROS/RNS (e.g., catalyzing superoxide elimination and inhibiting fenton reactions via metal chelation) and boosting endogenous defenses through autophagy/inflammatory pathway regulation.[12,26,27] Furthermore, PDA exhibits broad-spectrum adsorption affinity for inflammatory cytokines: electrostatic/hydrophobic interactions mediated by surface catechol/amino groups rapidly neutralize ≥21 inflammatory factors (e.g., >80% reduction in TNF-α/IL-6 within 24 h), providing immediate post-administration inflammation attenuation.[28] The bioadhesion with tissue components (like collagen) of PDA may further prolong localized drug retention, extending anti-inflammatory efficacy.[29]

Therefore, PDA was used to modify the surface of TAA NC in this research. Polydopamine-coated triamcinolone acetonide acetate nanocrystal (TAA@PDA) was supposed to prevent peritoneal adhesions through collectively yielding effects by TAA with PDA with multiple mechanisms including anti-inflammatory effect of TAA, ROS/RNS scavenging, certain hemostatic ability and adsorption of pro-inflammatory cytokines by numerous amino/phenolic hydroxyl groups of PDA (Scheme 1). The role of PDA coating was evaluated by comparing TAA@PDA with uncoated TAA NC both in vivo and in vitro with respect to the above properties.

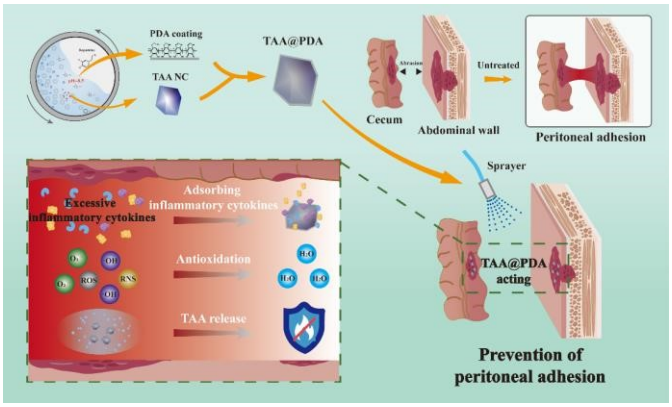

Scheme 1. Proposed PA-prevention mechanism of TAA@PDA.

Results and discussion

Characterization and morphology of TAA@PDA

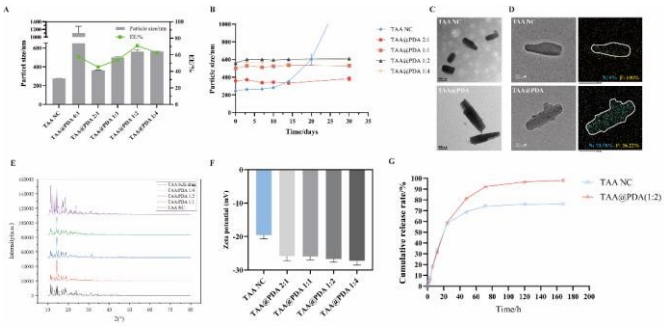

Fig.1 Physicochemical characterization of TAA@PDA: (A) influence of different feeding ratio on particle size and encapsulation efficiency; (B) stability (particle size vs. storage time); (C) TEM images; (D) EDS mapping (blue: Nitrogen, yellow: Fluorine); (E) XRD patterns; (F) zeta potential; (G) in vitro drug release profiles. (n=3, mean±SD)

Dopamine (DA) polymerization-based coating has emerged as excellent surface-adhesive materials due to their self-polymerization and interfacial adhesion capabilities.[30-32] Here, we employed one-step ball milling method to coat TAA NC with PDA: bulk TAA and dopamine were co-milled in a pH 8.5 environment, allowing dopamine to self-polymerize and form a surface coating during milling.

Using the above method, we successfully prepared TAA NC and TAA@PDA with different feeding ratios (TAA:DA, m/m) of 2:1, 1:1, 1:2, and 1:4 (Fig S1).

For particle size and encapsulation efficiency (Fig.1 A), TAA@PDA exhibited sizes of 364, 500, 560, and 564 nm and encapsulation efficiencies of 45%, 53%, 70%, and 65% at TAA:DA feeding ratios of 2:1, 1:1, 1:2, and 1:4, respectively, with both parameters increasing as the ratio decreased from 2:1 to 1:4 and peaking at 1:2 (Fig.1 A&Fig S3). We hypothesize this phenomenon stems from two factors: optimal ball milling efficiency at the 1:2 ratio, yielding more uniform grinding despite increased particle size; and surface coating saturation at 1:2, causing the observed maximum particle size.

For zeta potential (Fig.1 F), the values of TAA NC (-19.55 mV) and TAA@PDA at feeding ratios of 2:1, 1:1, 1:2, and 1:4 (-25.90, -26.00, -26.75, and -

27.25 mV, respectively) indicate that the surface zeta potential of PDA-coated TAA NC was significantly reduced compared with TAA NC. This change stems from deprotonation of PDA's phenolic hydroxyl groups (-OH) in solution, forming negatively charged phenoxide anions ($-O^-$) that boost surface negative charge density. The change in zeta potential also indirectly confirms the successful coating of PDA in TAA@PDA.

Notably, under different feeding ratios, PDA coating significantly enhanced the stability of TAA NC, maintaining dispersion stability for up to 30 days (Fig.1 B). In vitro release studies showed that PDA-coated TAA@PDA ensured complete drug release, whereas uncoated TAA NC ceased release after reaching 70% cumulative release (Fig.1 G). As the TAA:DA feeding ratio decreased from 2:1 to 1:4, the drug release only slowed slightly, exerting little impact on the drug release behavior (Fig S2). This improvement was attributed to the superior stability and reduced aggregation/precipitation of TAA@PDA compared to uncoated TAA NC.

X-Ray diffraction (XRD) analysis verified that PDA coating did not alter the crystalline structure of TAA nanocrystal (Fig.1 E). Transmission electron microscopy (TEM) revealed that TAA@PDA exhibited a rougher surface compared to uncoated TAA NC (Fig.1 C). The PDA coating of TAA@PDA introduces nitrogen (N) as a new characteristic element, which together with fluorine (F), the characteristic element of TAA, enables compositional confirmation. Elemental analysis showed that TAA NC contains 100% F (pure TAA), while TAA@PDA contains 73.78% N and 26.22% F confirming the presence of the PDA coating (Fig.1 D). Although EDS (energy dispersive dpectroscopy) mapping exhibits noise (an expected phenomenon for light elements N/F), the quantitative elemental data directly verifies the successful PDA coating.

Considering the above physicochemical properties and cell uptake promotion ability (Fig.6 C) (the TAA:DA ratio of 1:2 resulted in the highest encapsulation efficiency and strongest cell uptake promotion for TAA@PDA), the 1:2 ratio was selected for TAA@PDA preparation in subsequent experiments. Unless otherwise specified, 'TAA@PDA' hereinafter refers to polydopamine-coated nanocrystals prepared using a 1:2 TAA:DA feeding ratio.

Inflammatory cytokine adsorption

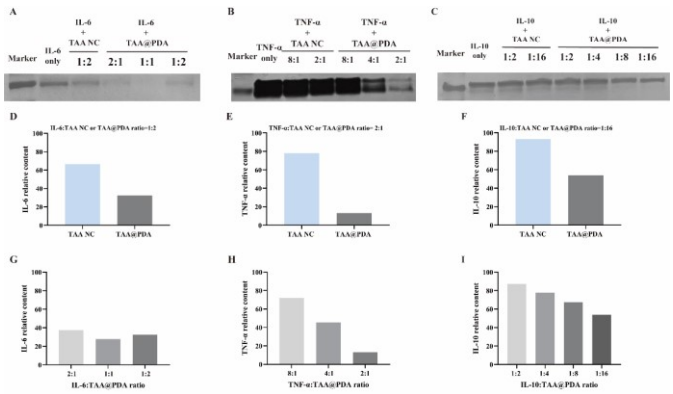

Fig.2 Influence of PDA coating (TAA@PDA vs TAA NC) on adsorption of cytokines by pro-inflammatory cytokine IL-6 (A), TNF-α (B) or anti-inflammatory cytokine IL-10 (C) shown by SDS-PAGE and their semi-quantitativeanalysis via grayscale intensity: IL-6 (D, G); TNF-α (E, H); IL-10 (F, I) (Note: ratio expressed as mass ratio).

Previous studies have established that PDA can broadly capture excessive cytokines in inflammatory microenvironments through physical adsorption.[28,33] Human neutrophils express TNF-α in response to IL-6 stimulation and TGF-β1 upon TNF-α stimulation, with TGF-β1$^+$ neutrophils triggering the adhesion process.[34] Interleukin-10 (IL-10), a key anti-inflammatory cytokine, potentially inhibits the activation of inflammatory cells such as neutrophils and macrophages, reduces the release of pro-inflammatory cytokines like TNF-α and IL-6, and thereby blocks the downstream TGF-β1-mediated fibrotic cascade—exerting a negative regulatory effect on the previously identified "IL-6→TNF-α→TGF-β1$^+$ neutrophils→adhesion formation" pathway.[35,36]

Given the critical roles of IL-6, TNF-α, and IL-10 in peritoneal adhesion formation, we hypothesize that PDA-mediated cytokine adsorption mitigates adhesion development. SDS-PAGE analysis and a semi-quantitative band gray value quantification revealed that TAA@PDA, compared to TAA NC, displayed enhanced adsorption of pro-inflammatory cytokines IL-6 and TNF-α alongside relatively limited binding to anti-inflammatory cytokine IL-10 (Fig.2). The selective adsorption may be related to the different structures of inflammatory cytokines, but the specific mechanism requires further in-depth exploration in future studies. This selective adsorption profile is particularly advantageous by possible reduction of pathogenic pro-inflammatory cytokines level and little influence on the beneficial anti-inflammatory cytokine, thereby interrupting the pro-adhesive inflammatory cascade triggered by tissue injury.

Interactions with collagen and tissue adhesion capacity

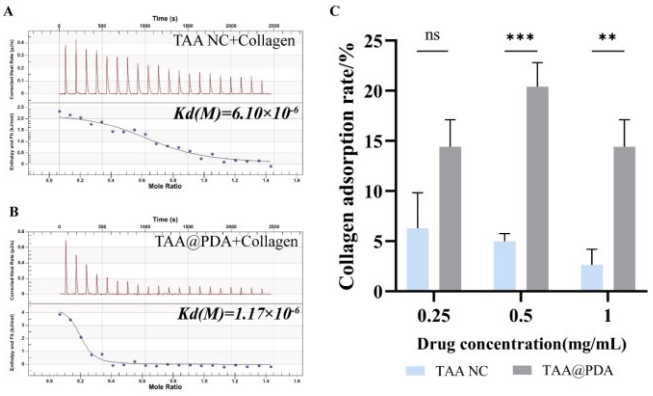

Fig.3 Influence of PDA coating on the interaction of nanocrystals with collagen (type I): (A,B) isothermal titration curves; (C) adsorption of collagen by TAA@PDA vs TAA NC at different drug concentrations (n=3, mean±SD). Statistical significance: *p<0.05, **p<0.01, ***p<0.001.

PDA is renowned for its exceptional tissue adhesion, attributed to its rich functional groups (quinones, catechols, imines, amines) and π-conjugated structures that enable robust interfacial bonding.[37] Collagen is widely distributed in the parietal peritoneum and visceral surfaces. Therefore, we evaluated the tissue adhesion properties of TAA@PDA by investigating its interaction with type I collagen.

Isothermal titration calorimetry (ITC) was used to determine the dissociation equilibrium constant (K_d), a key parameter quantifying binding affinity.[38] TAA@PDA displayed a significantly lower K_d value (1.17×10^{-6} mol/L) compared to TAA NC (6.10×10^{-6} mol/L), indicating stronger binding affinity to collagen (Fig.3 A&B). Equilibrium adsorption experiments using BCA protein quantification further confirmed that TAA@PDA exhibited significantly stronger collagen adsorption capacity than TAA NC. Quantitative results showed that the collagen adsorption amount of TAA@PDA was approximately 4-5 times that of TAA NC (Fig.3 C), which is fully consistent with the isothermal titration results. Such collagen affinity might enhance the retention of TAA@PDA at the injury site, facilitating localized drug delivery and sustained therapeutic effects at the injury site.

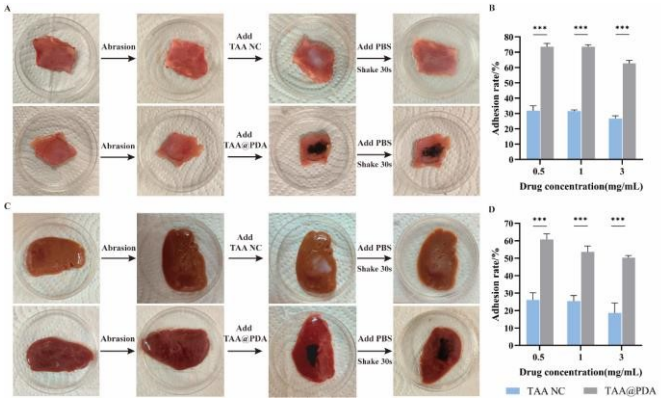

Fig.4 Tissue adhesiveness of TAA@PDA: (A) abdominal wall adhesion images; (B) abdominal wall adhesion rates at different concentrations; (C) liver adhesion images; (D) liver adhesion rates at different concentrations (n=3, mean±SD). Statistical significance: *p<0.05, **p<0.01, ***p<0.001.

To visually confirm the tissue adhesion of TAA@PDA, we performed tissue adhesion experiments using abraded rat abdominal walls and livers (Fig.4). Results demonstrated that TAA@PDA exhibited stronger adhesion to tissue surfaces compared to TAA NC. Specifically, TAA@PDA achieved 60%-70% and 50%-60% adhesion rates on abraded abdominal walls and livers, respectively, significantly higher than the 20%-30% observed with TAA NC. This effective adhesion promotes the retention of TAA@PDA at post-surgical wounds, enabling better exertion of its antioxidant and anti-inflammatory effects to prevent peritoneal adhesion formation.

Extracellular antioxidant capacity

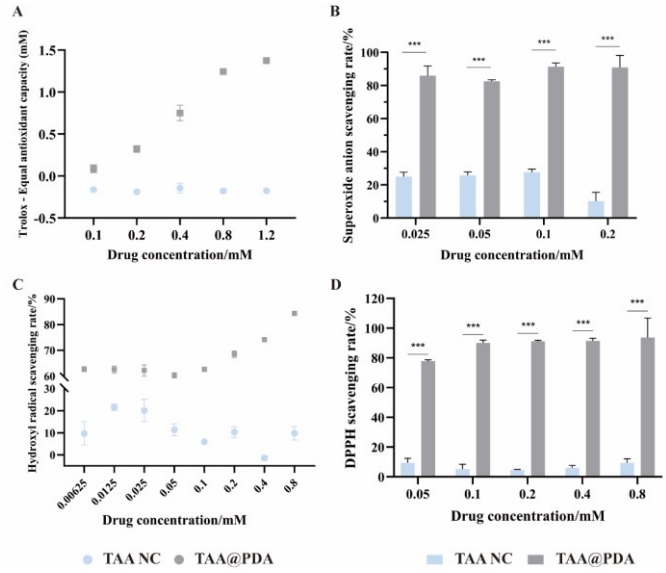

Fig.5 Influence of PDA coating on antioxidant properties of TAA@PDA: (A) total antioxidant capacity; (B) superoxide anion scavenging activity; (C) hydroxyl radical scavenging activity; (D) DPPH scavenging activity. (n=3, mean±SD) Statistical significance: *p<0.05, **p<0.01, ***p<0.001.

Intraoperative procedures such as incision, electrocautery, and ligation inevitably damage the vascular system, leading to local tissue hypoxia, accumulation of metabolic byproducts (e.g., lactic acid), and decreased pH.[39] These insults force cells to switch from aerobic to anaerobic metabolism, triggering oxidative stress pathways that generate excessive ROS. This oxidative burst upregulates specific inflammatory cytokines—key mediators of the "inflammatory cascade" that initiates adhesion formation.[40] Consequently, efficient radical scavenging has emerged as a critical therapeutic target for blocking peritoneal adhesion pathogenesis. PDA-based materials have exhibited good radical scavenging capacity due to their unique catechol moieties.

To evaluate the antioxidant capacity of TAA@PDA, multiple assays were employed to determine its scavenging efficiency against ROS. ABTS assays confirmed that TAA@PDA possessed concentration-dependent potent antioxidant activity (Fig.5 A). Further radical scavenging experiments demonstrated that TAA@PDA achieved nearly 80% clearance efficiency for hydroxyl radicals, superoxide anions, and DPPH (Fig.5 B&C&D), making the interruption of "oxidative stress initiation switch" during early adhesion development possible by neutralizing excessive radicals.

Cytotoxicity and cell uptake

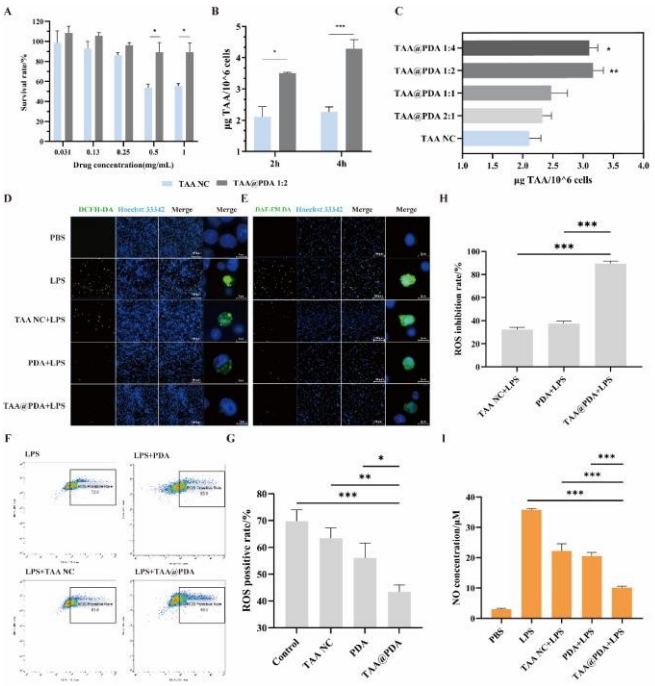

Fig.6 Influence of PDA coating on TAA@PDA' cellular response: (A) cytotoxicity (CCK-8); (B) uptake efficiency of TAA@PDA by RAW 264.7 cells at 2h/4h (drug concentration=50 μg/mL); (C) comparison of RAW 264.7 cellular uptake of TAA@PDA with different feeding ratios (drug concentration=50 μg/mL); (D) ROS fluorescent staining (DCFH-DA and drug concentration=50 μg/mL); (E) NO fluorescent staining (DAF-FM DA and drug concentration=50 μg/mL); (F) flow cytometry ROS positive rate and (G) quantitative analysis (drug concentration=50 μg/mL); (H) ROS inhibition rate (microplate reader)(drug concentration=50 μg/mL); (I) NO secretion level (drug concentration=100 μg/mL). (n=3, mean±SD) Statistical significance: *p<0.05, **p<0.01, ***p<0.001.

CCK-8 assays confirmed the negligible cytotoxicity of TAA@PDA (Fig.6 A). Cell viability and cytotoxicity staining yielded consistent results (Fig S4). At high TAA concentrations, PDA coating significantly mitigated the potential cytotoxicity of the drug. This effect may be attributed to the delayed drug release conferred by the PDA coating and a protective role of PDA toward the cells. The presence of Tween 80 in TAA NC suspension also exacerbates its cytotoxicity. Overall, PDA coating could potentially prevent damage to immune cells, thereby enhancing safety. The concentrations used in subsequent experiments were all below the cytotoxic concentration of TAA NC, thus essentially ruling out potential interference from drug-induced cytotoxicity on the experimental results.

Cellular uptake results (Fig.6 B&C) demonstrated that PDA coating significantly promoted cellular uptake, and the cellular uptake efficiency gradually enhanced as the TAA:DA feeding ratio decreased from 2:1 to 1:4, reaching its peak at a ratio of 1:2. This might be explained by the chemical structure of PDA rich in catechol groups (o-dihydroxybenzene) which are capable of interacting with extracellular matrix proteins (such as collagen and laminin) via covalent bonds or hydrogen bonds.[41]

Intracellular antioxidant and anti-inflammatory activities

Intracellular ROS acts as a "double-edged sword". At physiological concentrations, ROS functions as signaling molecules to regulate immune activation and inflammatory balance, while excessive ROS accumulation triggers oxidative stress, leading to biomolecular damage and inflammatory pathway activation that exacerbate disease progression.[42,43] In the pathological process of peritoneal adhesion, overproduction of ROS disrupts peritoneal integrity through direct oxidative damage and indirect signal transduction, activates fibrotic pathways, and exacerbates inflammatory responses, forming a vicious cycle.[44]

The antioxidant and anti-inflammatory activities of TAA@PDA were evaluated in an LPS-induced ROS-overproducing RAW 264.7 cells and visualized using the DCFH-DA fluorescent probe. Confocal microscopy results (Fig.6 D) showed that the intracellular green fluorescence intensity in the TAA@PDA + LPS group was significantly lower than that in the LPS-only group, as well as lower than both the TAA NC + LPS group and PDA + LPS group, indicating effective intracellular ROS scavenging by TAA@PDA. Further quantitative analysis via flow cytometry revealed the lowest ROS-positive cell rate in TAA@PDA-treated samples (Fig.6 F&G), while microplate reader assays confirmed the highest ROS scavenging rate—approximately equivalent to the sum of effects observed with TAA NC and PDA alone (Fig.6 H). This confirms the action of the "core-shell" structure, attributed to the combined effects of the PDA coating's direct free radical scavenging capacity and the TAA nanocore's anti-inflammatory properties.

ROS and NO serve as critical markers of inflammation and oxidative stress, with their over-expression levels reflecting cellular damage severity.[45] Aberrant activation of inducible nitric oxide synthase (iNOS) under inflammatory stimulation represents another critical pathological link. The excessive NO generated by iNOS catalysis can react with superoxide anions to form highly oxidizing peroxynitrite ($ONOO^-$), triggering nitrosative stress responses that ultimately result in apoptosis, inflammatory cascade amplification, and DNA damage.[46]

To verify TAA@PDA's regulatory effect on NO production, experiments induced high iNOS expression via LPS and employed 4-amino-5-methylamino-2',7'-difluorofluorescein diacetate (DAF-FM DA) probe for visualization. Confocal imaging with DAF-FM-DA staining showed that TAA@PDA significantly inhibited LPS-induced intracellular NO production (Fig.6 E). NO secretion quantification assays further verified TAA@PDA's ability to reduce extracellular NO levels (Fig.6 I). NO is both a typical inflammatory cytokine and a representative reactive nitrogen species (RNS). The above results demonstrate the potent anti-inflammatory effect of TAA@PDA, as well as its inhibitory and scavenging capabilities against RNS production.

Collectively, these findings demonstrate that TAA@PDA achieves dual regulation of "antioxidant-anti-inflammatory" effects by simultaneously inhibiting NO secretion and scavenging ROS/RNS, providing experimental evidence for its potential application in inflammatory disease therapy.

Hemostatic activity assay

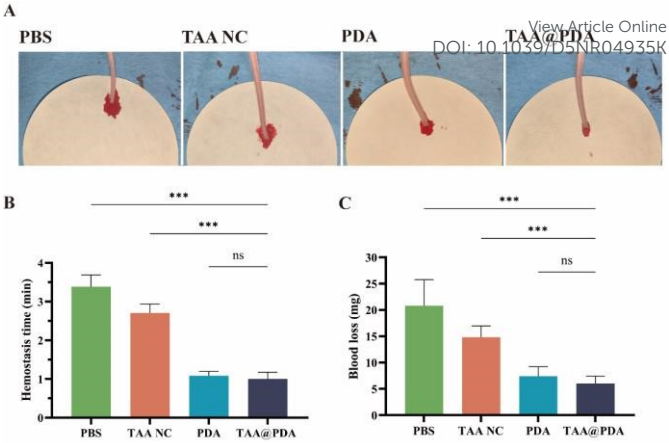

Fig.7 Characterization of hemostatic efficacy: (A) representative experimental images, (B) hemostasis time, and (C) blood loss mass (n=4, mean±SD). Statistical significance: *p<0.05, **p<0.01, ***p<0.001.

As shown in Fig.7, in the mouse tail amputation model, both the TAA@PDA and PDA groups exhibited the shortest bleeding time and the lowest blood loss volume, indicating the optimal hemostatic efficacy. In contrast, the TAA NC group showed almost no hemostatic capability. The hemostatic capability of PDA may be primarily due to its adhesiveness, which facilitates wound sealing and concurrently promotes blood cell aggregation to initiate hemostasis.[47] In the context of abdominal adhesion prevention, surgical procedures often involve minor wound bleeding. The inherent hemostatic ability of PDA can reduce the local deposition of blood-derived fibrous tissue, thereby lowering the risk of adhesion formation.

In vivo antiadhesive efficacy of TAA@PDA

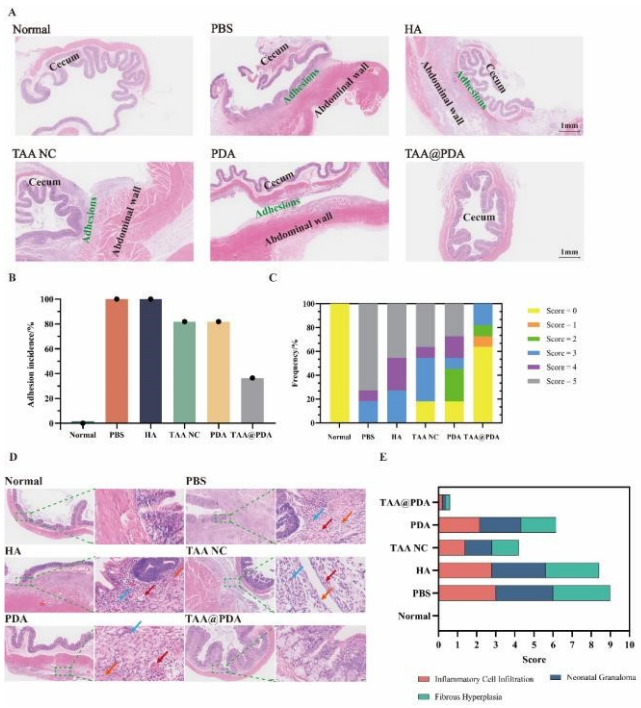

Fig.8 Therapeutic efficacy of TAA@PDA in a rat peritoneal adhesion model: (A) adhesion tissue HE staining; (B) adhesion incidence (n=11); (C) adhesion score (n=11); (D) typical 20× HE-staining for pathological analysis (orange arrow: connective tissue hyperplasia; blue arrow: inflammatory cell infiltration; red arrow: neovascularization); (E) pathological score (n=6).

In this study, a classical intraperitoneal adhesion model was established by injuring the cecum and peritoneum.[48] The treatment group received TAA@PDA administered via a miniature spray device at the injury site to evaluate its preventive effects on peritoneal repair and adhesion. The administration device is a disposable ENT (Ear, Nose, and Throat) sprayer (Fig S5), primarily composed of a connector (for attaching to the syringe), connecting tube (for fluid delivery), and spray nozzle (for generating the aerosol). In use, it connects to a syringe containing the formulation, with spray delivery achieved by generating pressure through pushing the syringe. Delivery via spray enables uniform distribution of TAA@PDA at tissue injury sites, ensuring the efficacy of peritoneal adhesion prevention.

One week post-surgery, exploration revealed severe adhesion in both the PBS (model) group and the commercial hyaluronic acid (HA) group, with firm fibrous bands forming between the cecum and peritoneum that could not be separated by gentle traction, indicating progression to permanent adhesions. In contrast, most animals in the TAA@PDA group exhibited no adhesions, suggesting superior preventive efficacy (Fig.8 A&Fig S6). Adhesion scoring further confirmed the optimal performance of TAA@PDA, with an adhesion incidence of only 36.4% and a low severe adhesion incidence of 9.1% (score ≥ 4), whereas both the TAA NC and PDA groups showed an adhesion rate of 81.8% and a severe adhesion rate of 45.4%; both the commercial HA and PBS groups reached 100% adhesion incidence, with severe adhesion rates of 72.7% and 81.8%, respectively (Fig.8 B&C, Table S1).

Pathological analysis demonstrated that the TAA@PDA group had significantly reduced inflammatory cell infiltration, granuloma formation, and fibrosis in cecal tissues by pathological score (Fig.8 D&E, Table S2&S3&S4). Furthermore, ELISA results demonstrated that TAA@PDA treatment significantly reduced serum levels of the inflammatory cytokines IL-6 and TNF-α (Fig S7), which have been shown to trigger adhesion in peritoneal adhesions by promoting neutrophil expression of TGF-β1. Immunohistochemical analysis demonstrated that TAA@PDA significantly reduced the distribution of α-SMA and TGF-β1 at the cecal injury site, which correlated with its anti-adhesion properties (Fig.9 C-F). This improvement was associated with TAA's anti-inflammatory action and the PDA shell's antioxidant properties, which together effectively suppressed oxidative stress and excessive inflammatory responses during the initial adhesion phase.

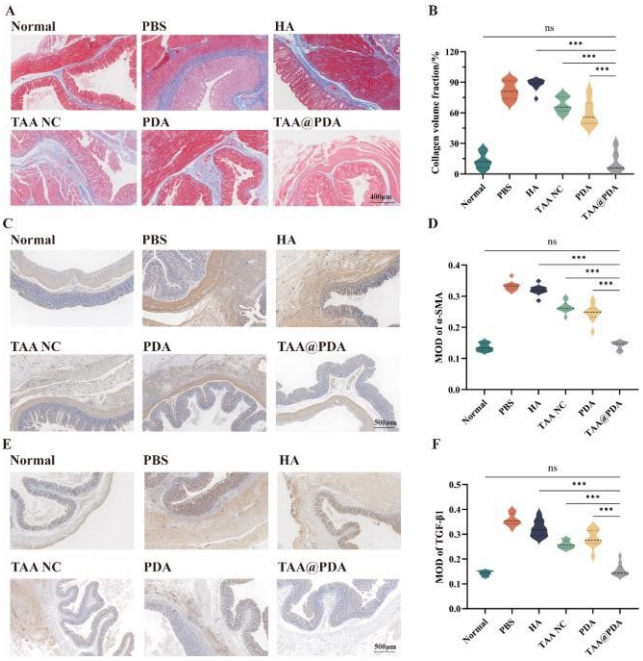

Fig.9 Masson staining and immunohistochemical analysis of each experimental group: (A) representative masson collagen staining micrographs; (B) collagen volume fraction; (C) representative α-SMA immunostaining micrographs; (D) semi-quantitative evaluation of α-SMA expression; (E) representative TGF-β1 immunostaining micrographs; (F) semi-quantitative evaluation of TGF-β1 expression. (n=10) Statistical significance: *p<0.05, **p<0.01, ***p<0.001.

Macrophages regulate peritoneal repair through the balance of M1/M2 polarization, where M1 macrophages promote inflammation and adhesion formation, while M2 macrophages inhibit excessive inflammation and promote orderly repair to reduce the risk of adhesion.[49] Immunohistochemical results showed that both the PDA and TAA@PDA significantly increased the M2/M1 ratio; however, the M2/M1 ratio in the HA group was even lower than that in the model group, suggesting that physical barrier materials may interfere with macrophage function and exacerbate inflammation (Fig S8). The M2-polarizing effect of TAA@PDA likely stems from its dual capacity to scavenge ROS and mitigate inflammation. PDA can scavenge ROS and alleviate oxidative stress, thereby inhibiting the activation of pro-inflammatory signaling pathways such as NF-κB, and fostering an anti-inflammatory microenvironment conducive to M2 polarization.[50,51] This ability to promote M2-type macrophage polarization enhances its anti-inflammatory effects.

Collagen deposition, as a core pathological basis of adhesion, disrupts peritoneal repair balance, leading to permanent fibrotic scarring. Masson staining indicated markedly controlled collagen volume fraction and alleviated collagen deposition in the TAA@PDA group (Fig.9 A&B), corroborating its role in delaying fibrosis by regulating fibroblast activation and extracellular matrix degradation.

Observations of rats on days 1, 3, 5, and 7 post-administration revealed that TAA@PDA continuously adhered to and retained at peritoneal and cecal injury sites throughout the 7-day period (Fig S9). Although the retention amount gradually decreased over time, a relatively high level was consistently maintained within the first 3 days. This dynamic change is closely associated with the repair process at the injury site, physiological flushing within the abdominal cavity, and the inherent degradation of TAA@PDA. Considering the dynamic nature of postoperative peritoneal adhesion formation, the first three days are dominated by inflammatory responses with intensified oxidative stress, during which fibrinogen begins to deposit and convert into fibrin.[1,34] This period thus represents the "golden time window" for preventing peritoneal adhesions. The long-term retention property of TAA@PDA can fully cover this pathological window, thereby exerting a sustained adhesion-preventing effect.

Histopathological examination revealed no obvious toxic damage in major organ sections (Fig.10 E), together with body weight time-profiles and complete blood count result (Fig S10&Fig.10 A-D), confirming good biocompatibility of TAA@PDA. The hemolysis evaluation results showed that TAA@PDA exhibited hemolysis rates below 5%, indicating no significant hemolytic activity (Fig S11). In contrast, the TAA NC groups displayed hemolysis rates exceeding 10% across all tested concentrations, demonstrating the superior blood safety profile of TAA@PDA.

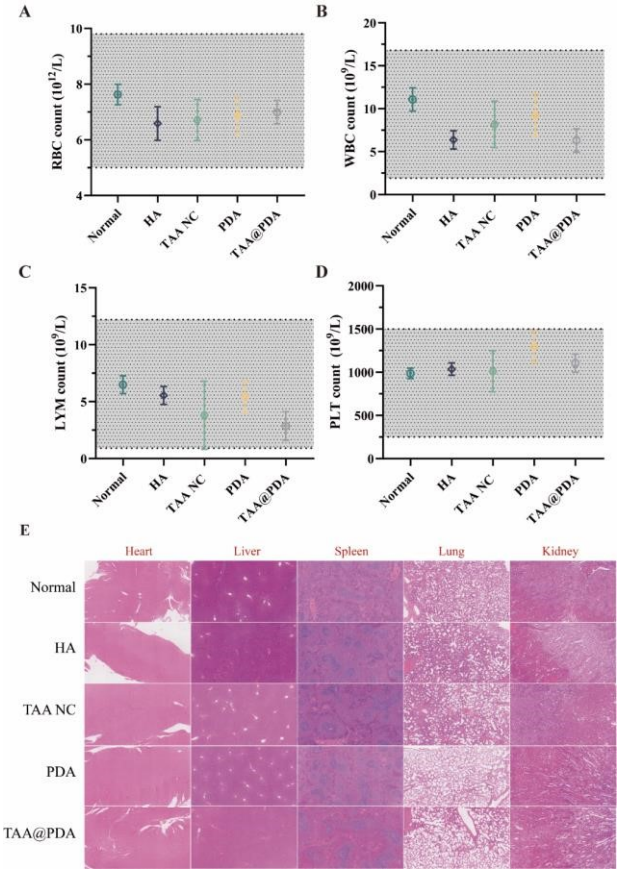

Fig.10 Biosafety evaluation of TAA@PDA: (A) red blood cells (RBC); (B) white blood cells (WBC); (C) lymphocytes (LYM); (D) platelets (PLT) in rats after 7-day treatment (n=4, mean±SD); (E) representative HE-stained sections of major organs (20× magnification).

Materials and methods

Materials

Chemicals and solvents were purchased from Sinopharm Chemical Reagent Co., Ltd (Shanghai, China). Triamcinolone acetonide acetate, dopamine hydrochloride, type I collagen and DPPH were purchased from Meilun Biotechnology (Shanghai, China). The 1 mm zirconia grinding beads were purchased from Torray Industries (Tokyo, Japan). Interleukin-6 and interleukin-10 were purchased from Yuli Biotechnology (Shanghai, China). The BCA protein assay kit, total antioxidant capacity detection kit (ABTS method), cell counting kit-8 (CCK-8 kit) , cell viability and cytotoxicity assay kit, DCFH-DA and DAF-FM DA were purchased from Beyotime Biotechnology (Shanghai, China). The medical hyaluronic acid gel was obtained from Zhejiang Jingjia Medical Technology Co., Ltd. (Zhejiang, China). Disposable ENT (Ear, Nose, and Throat) anesthetic sprayer was purchased from Tuoren Best Medical Device Co., Ltd. (Henan, China).

RAW 264.7 murine macrophage cells were obtained from the Shanghai Cell Bank of the Chinese Academy of Sciences. The cell line was cultured in Dulbecco's Modified Eagle Medium (DMEM; Gibco, Thermo Fisher Scientific, Waltham, MA, USA) supplemented with 10% fetal bovine serum (FBS; Gibco, Thermo Fisher Scientific), 100 units/mL penicillin, and 100 μg/mL streptomycin. Cultures were maintained at 37°C in a humidified atmosphere containing 5% carbon dioxide.

Male Sprague-Dawley rats (8 weeks of age, 200-250g) and male ICR mice (7 weeks of age, 20-23g) were procured from the Shanghai Laboratory Animal Center (Shanghai, China). All animal procedures were performed in accordance with the Regulations on the Administration of Laboratory Animals of the People's Republic of China and the Guidelines for Care and Use of Laboratory Animals of Fudan University, and were approved by the Animal Ethics Committee of Fudan University.

Unless otherwise specified, all concentrations of TAA NC or TAA@PDA mentioned in this article are calculated based on the TAA drug concentration, and no additional explanations will be provided hereafter.

Preparation and Characterization of TAA@PDA

TAA powder and Tween 80 were added into a ball milling jar at a drug-to-stabilizer mass ratio of 5:1, followed by milling at 400 rpm for 4 h to obtain TAA NC. For TAA@PDA preparation, TAA powder and dopamine hydrochloride were mixed in a ball milling jar at specific feeding ratios (TAA:DA, m/m) and milled under identical conditions (400 rpm, 4 h). When preparing TAA@PDA with varying TAA:DA feeding ratios, maintain a constant TAA dosage while gradually increasing DA input to decrease the TAA:DA ratio from 2:1 to 1:4. To characterize the PDA coating, TEM imaging was conducted on TAA NC and TAA@PDA, with concurrent EDS-mapping analysis of fluorine (F, a characteristic element of TAA) and nitrogen (N, a characteristic element of PDA) distributions. The particle size and zeta potential of TAA@PDA were measured using a malvern particle size analyzer. XRD was employed for crystal form analysis of TAA@PDA. The in vitro release properties of TAA NC and TAA@PDA with different TAA:DA feeding ratios were determined in 2% Tween 80 solution.

Inflammatory cytokine adsorption by TAA@PDA

To verify the physical adsorption of inflammatory cytokines by PDA for local inflammation mitigation, TAA@PDA or TAA NC was co-incubated with IL-6, TNF-α, and IL-10 at various mass ratios at 37°C for 3 h. Nanoparticles were then removed by centrifugation at 10000 rpm, and the residual protein content in supernatants was visualized via SDS-PAGE gel electrophoresis followed by staining to evaluate adsorption capacity. Subsequently, semi-quantitative grayscale analysis of gel bands was performed using ImageJ software. Relative inflammatory cytokine content = Ge/Gc×100, where Ge = grayscale value of the experimental group band (inflammatory cytokine + TAA NC or TAA@PDA), Gc = grayscale value of the control group band (inflammatory cytokine only).

Interactions with collagen and tissue adhesion capacity

ITC was used to measure the dissociation equilibrium constant (Kd) between TAA@PDA/TAA NC and collagen. Additionally, TAA NC or TAA@PDA was co-incubated with type I collagen at 37°C, followed by centrifugation at 10000 rpm for 15 min to remove nanoparticles. The residual protein concentration in supernatants was quantified using a BCA protein assay kit to calculate the collagen adsorption capacity of the formulations. Collagen adsorption rate (%) = (Initial collagen content - Residual collagen content) / Initial collagen content × 100%.

The rat abdominal wall or liver was physically abraded, rinsed with PBS (pH 7.4), and then placed in a culture dish. Then, TAA NC or TAA@PDA was dropped onto the abraded wound and allowed to stand for 1 min. PBS (37°C) was then added, and after gently shaking the culture dish, the samples on the organs were imaged, and the samples detached in PBS were collected. The drug content in these samples was measured by HPLC to calculate the tissue adhesion rate. Adhesion rate (%) = (Adsorbed amount / Applied amount) × 100%.

Extracellular antioxidant capacity

Total antioxidant capacity was measured using an ABTS assay kit, based on the decolorization of ABTS radical cations (ABTS•+). Trolox standard solution was diluted to 0.15–1.5 mM to generate a standard curve. In a 96-well plate, 200 μL ABTS working solution was added to each well, followed by 10 μL ultrapure water (blank), Trolox standards, or TAA@PDA/TAA NC (samples). After 5-min incubation at room temperature, absorbance at 734 nm was measured. The total antioxidant capacity was calculated via the standard curve and expressed as Trolox-Equivalent Antioxidant Capacity (TEAC) in equivalent Trolox concentration.[52]

For hydroxyl radical (HO•) scavenging efficiency, a fluorescent probe method was utilized: Reaction systems containing 0.5 mM terephthalic acid (TA), 10 mM H_2O_2, and serial concentrations of TAA@PDA or TAA NC were prepared in PBS (pH 7.4). TA itself is non-fluorescent, but reacts with HO• to form 2-hydroxyterephthalic acid, which exhibits characteristic fluorescence (Ex: 320 nm, Em: 425 nm). After incubation at 37°C for 12 h in the dark, nanoparticles were removed by centrifugation at 12000 rpm for 5 min. HO• scavenging efficiency was indirectly assessed by measuring the fluorescence intensity of supernatants using a fluorospectrophotometer. Scavenging efficiency (%) = [1 - (F_{sample} - F_{blank}) / ($F_{control}$-F_{blank})] × 100%, where F_{sample} = fluorescence intensity of the experimental reaction system containing TAA@PDA or TAA NC, $F_{control}$ = fluorescence intensity of the positive control system (HO• generation without scavengers), F_{blank} = fluorescence intensity of the blank system (PBS buffer + TA only, accounting for background fluorescence without HO• and nanoparticles).

Superoxide anion ($O_2^{\bullet-}$) scavenging capacity was evaluated via the nitro blue tetrazolium (NBT) photoreduction inhibition assay: Systems containing 20 μM riboflavin, 12.5 mM methionine, 75 μM NBT, and various concentrations of TAA@PDA or TAA NC were prepared in PBS (pH 7.4). Riboflavin generates $O_2^{\bullet-}$ upon UV irradiation, which reduces NBT to form blue formazan (characteristic absorption at 560 nm). After 15 min of UV exposure, absorbance at 560 nm was measured. Three groups were set: sample group (UV-irradiated with TAA@PDA or TAA NC), positive control (UV-irradiated), and negative control (non-irradiated complete system). Inhibition rate was calculated using the formula: Inhibition rate (%) = [(A_0 - A_n)/(A_p - A_n)] × 100%, where A_0, A_n, and A_p represent absorbance of the sample group, negative control, and positive control, respectively.

The DPPH radical scavenging assay was performed as follows: Equal volumes of 0.2 mM DPPH working solution and serial concentrations of TAA@PDA or TAA NC were mixed, reacted for 30 min at room temperature in the dark, and absorbance at 517 nm was measured. DPPH radicals, which exhibit a purple color, undergo discoloration upon scavenging, resulting in decreased absorbance. DPPH mixed with 95% ethanol served as the positive control, while TAA@PDA or TAA NC mixed with 95% ethanol was the negative control. Scavenging rate was calculated as: Scavenging rate (%) = [1 - (A_i - A_j)/Ac] × 100% where A_i, A_j, and Ac denote absorbance of the sample group, negative control, and positive control, respectively.

Cytotoxicity and cell uptake

In the cytotoxicity experiment, RAW 264.7 cells were seeded in 96-well plates at a density of 5×10^5 cells/mL with a volume of 100 μL per well. The plates were pre-incubated at 37°C in a 5% CO_2 humidified incubator for 12 h to allow complete cell adherence. After discarding the original medium, fresh medium containing TAA@PDA or TAA NC at various concentrations was added to each well, followed by an additional 24-hour incubation. The medium was then aspirated, and cells were gently washed three times with PBS (pH 7.4). Subsequently, 10 μL of CCK-8 solution was added to each well, and the plates were returned to the incubator for 1-hour incubation. Absorbance at 450 nm was measured using a microplate reader. Cell viability was calculated using the formula: Cell viability (%) = [(As - Ab) / (Ac - Ab)] × 100%, where: As = absorbance of experimental wells (with cells, medium, CCK-8, and TAA@PDA/TAA NC); Ac = absorbance of control wells (with cells, medium, CCK-8); Ab = absorbance of blank wells (with medium and CCK-8 only). Meanwhile, cells from each treatment group were stained using a Calcein/PI cell viability and cytotoxicity assay kit to visually assess cell viability.

In the cell uptake experiment, RAW 264.7 cells were plated in 6-well plates and cultured at 37°C for 12 h until adherence. After confirming good cell morphology via microscopy, the original medium was replaced with fresh medium containing the TAA@PDA or TAA NC (final TAA concentration: 50 μg/mL). Following incubation at 37°C for 2 or 4 h, the culture medium was aspirated, and 1 mL of cold PBS was added to detach cells via gentle pipetting. Cell suspensions were counted and then centrifuged at 1000 rpm for 5 min. The cell pellet was resuspended in 1 mL PBS, and this washing step was repeated three times. Cells were lysed by probe sonication (90 W, 2 s on/2 s off, 6 cycles), followed by addition of acetonitrile, vortexing for 1 min, and centrifugation at 8000 rpm for 15 min. The supernatant was collected for HPLC analysis. Cellular uptake was calculated as: Cellular uptake (μg/10^6 cells) = Drug content / Cell number.

Intracellular antioxidant and anti-inflammatory activities

RAW 264.7 macrophages were seeded into 24-well plates at a density of 5×10^4 cells/well and cultured at 37°C with 5% CO_2 for 24 h before treatment. The experiment was divided into 5 groups: control group (basic medium only); LPS model group (stimulated with 1 μg/mL LPS); LPS+PDA group (1 μg/mL LPS + 25 μg/mL PDA, corresponding to the PDA content contained in TAA@PDA); LPS+TAA@PDA group (1 μg/mL LPS + 50 μg/mL TAA@PDA); and LPS + TAA NC group (1 μg/mL LPS + 50 μg/mL TAA NC). All treatments were administered for 24 h.

After treatment, the supernatant was discarded, and cells were gently washed 3 times with PBS (pH 7.4) to remove residual drugs. Each well was incubated with 500 μL of 10 μM DCFH-DA probe solution (diluted in serum-free medium) at 37°C for 30 min in the dark. Following incubation, cells were washed 3 times with PBS to eliminate background fluorescence interference. Fluorescence intensity was measured using a microplate reader (excitation: 485 nm, emission: 525 nm), and the proportion of ROS-positive cells was quantified by flow cytometry. Laser confocal microscopy was used to observe intracellular ROS distribution. The ROS inhibition rate was calculated using the formula: ROS inhibition rate (%) = (F_{lps} - $F_{treatment}$)/(F_{lps} - $F_{control}$) × 100%, where F_{lps} represents the fluorescence intensity of the LPS model group, $F_{treatment}$ represents the fluorescence intensity of the treatment groups, and $F_{control}$ represents the fluorescence intensity of the control group.

As for NO production inhibition assay, cell seeding density and grouping were identical to the ROS detection assay.[53] After 24-hour drug treatment, cell culture supernatants were collected for NO measurement using the total nitric oxide assay kit. Briefly, 100 μL of supernatant was mixed with equal volumes of Griess Reagent I and II, incubated at room temperature for 15 min in the dark, and absorbance was measured at 540 nm using a microplate reader. NO_2^- concentration (representing NO production) was calculated from a sodium nitrite standard curve.

For visual validation, parallel experiments were performed: after 24-hour treatment, cells were washed with PBS and incubated with 5 μM DAF-FM-DA probe solution at 37°C for 20 min in the dark. Following 3 PBS washes, laser

confocal microscopy was used to observe fluorescence distribution (excitation: 495 nm, emission: 515 nm).

Hemolytic activity

Fresh whole blood from SD rats was centrifuged at 1500 rpm for 10 min, and the supernatant was discarded. After washing three times with PBS (pH 7.4), the pellet was resuspended to prepare a red blood cell (RBC) suspension. The RBC suspension was mixed with serial concentrations of TAA NC or TAA@PDA suspensions and incubated at 37°C for 2 h. After incubation, the mixture was centrifuged at 1500 rpm for 10 min to collect the supernatant, which was further centrifuged at 10000 rpm for 10 min to remove residual nanoparticles. The absorbance of the supernatant was measured at 542 nm. PBS served as the negative control (0% hemolysis) and ultrapure water as the positive control (100% hemolysis). Hemolysis rate was calculated using the formula: Hemolysis Rate (%) = $[(A_{Sample} - A_{Negative}) / (A_{Positive} - A_{Negative})] \times 100\%$ (A_{Sample}: absorbance of sample group; $A_{Negative}$: absorbance of PBS control; $A_{Positive}$: absorbance of ultrapure water control).

Hemostatic activity assay

The hemostatic capacity of TAA@PDA was evaluated by measuring blood loss and hemostatic time in a mouse tail amputation model. ICR mice were randomly divided into four groups. After anesthesia, the mouse tail was transected approximately 1.0 cm from the tip using a surgical scalpel to create a bleeding wound. Immediately after amputation, TAA NC, TAA@PDA (1 mg/mL) or PDA suspension (0.5 mg/mL, corresponding to the PDA content contained in TAA@PDA) was sprayed onto the bleeding site. A pre-weighed filter paper was placed beneath the tail to absorb the shed blood. Hemostatic time was recorded with a timer when no bleeding was visually observed. The filter paper containing absorbed blood was then weighed to calculate the total blood loss. Wounds receiving PBS (pH 7.4) served as the blank control.

In vivo antiadhesive efficacy of TAA@PDA

SD rats were employed to establish a cecal abrasion model for evaluating the anti-adhesion efficacy of TAA@PDA in vivo.[54] Prior to surgery, the abdominal hair was shaved, and a 4–5 cm incision was made along the midline. After opening the abdominal cavity, the cecum was gently exposed and abraded repeatedly with dry gauze until petechial hemorrhages appeared, creating a wound area of approximately 3 cm × 2 cm. Simultaneously, a 3 cm × 1.5 cm abdominal wall defect was created on the lateral abdominal wall using a surgical blade, with abrasion depth reaching the muscle layer to improve modeling success.

A small spray device was used to uniformly apply the TAA@PDA suspension to the injured area at a dosage of 0.5 mg/kg. The other experimental groups were designed as follows: the TAA NC group received the same dosage of TAA NC, the PDA group received the corresponding concentration of PDA (corresponding to the PDA content contained in TAA@PDA), the commercial preparation group received 0.6 mL of medical HA gel, the PBS group received an equal volume of PBS (pH 7.4), the normal group underwent sham operation (only laparotomy and closure without cecal abrasion or abdominal wall defect).

During the 7-day treatment period, partial rats were dissected on days 1, 3, 5, and 7 respectively, followed by photography to observe the retention of TAA@PDA at the injury site.

On the 7th day post-surgery, the abdominal cavity was reopened to observe and score the extent of adhesion between the cecum and the abdominal wall according to a standardized adhesion scoring system. The adhesion incidence (Score > 0) and severe adhesion incidence (Score > 3) were calculated. Adhesion and related tissue samples were collected for histological analysis: HE staining was used to observe tissue morphology, masson staining was applied to evaluate collagen fiber deposition, and immunohistochemistry was employed to determine the expression levels of α-SMA, TGF-β1, CD86 and CD206 at the adhesion sites. For semi-quantitative analysis of masson staining, the collagen volume fraction (CVF) was calculated as: CVF (%) = (Collagen-positive Area / Total Tissue Area)×100%. And for immunohistochemistry of α-SMA and TGF-β1, the Mean Optical Density (MOD) was used to represent the protein-positive expression level in tissues. MOD refers to the average optical density value of all positive pixels within a selected region of interest, calculated by dividing the Integrated Optical Density (IOD) by the area of the region being measured. In the immunohistochemical detection of CD206 and CD86, the M2/M1 polarization ratio was calculated using the formula: M2/M1 ratio = ($CD206^+$ cells/mm²) / ($CD86^+$ cells/mm²). CD86 and CD206 are markers for M1 and M2 macrophages, respectively. These analyses were conducted using the imageJ software.

Statistical analysis

Data were analyzed using GraphPad Prism 10. Results are presented as mean±standard deviation (SD). Two-tailed unpaired Student's t-test was used for comparisons between two groups, while one-way analysis of variance (ANOVA) followed by Tukey's multiple comparisons test was applied for multiple group comparisons. Statistical significance was set at $p < 0.05$. *$p < 0.05$, **$p < 0.01$, and ***$p < 0.001$.

Conclusion

In this study, TAA@PDA was successfully prepared by the one-step wet media milling method to coating PDA on the surface of TAA nanocrystals. It not only reduced the accumulation of inflammatory cytokines at the injury site but also effectively alleviated cellular oxidative stress. Its moderate hemostatic capacity and ability to promote macrophage M2 polarization further enable effective prevention of peritoneal adhesions. Its capability to inhibit collagen deposition, the inflammatory state, and thus peritoneal adhesion was proven in animal models of peritoneal adhesion. These findings shed light on such a novel peritoneal adhesion prevention strategy by combining beneficial effects of TAA and PDA, and provided an efficient solution to prevent postoperative peritoneal adhesion for clinical application. In future studies, we will conduct more in-depth and comprehensive research on the therapeutic mechanism of TAA@PDA.

Author contributions

Conceptualization: Yu Liu, Y.J., H.L.; Investigation: Yaodong Liu, C.L.; Methodology: Yaodong Liu, S.L., D.J.; Data Curation: Yaodong Liu; Visualization: Yaodong Liu, D.J.; Writing-Original Draft: Yaodong Liu; Writing-Review & Editing: Yaodong Liu, D.J., S.L., C.L., Y.J., H.L., X.Q.,Yu Liu; Resources: Yu Liu, Y.L.; Supervision: Yu Liu, Y.J.; Project Administration: Yu Liu.

Conflicts of interest

There are no conflicts to declare.

Data availability

The data supporting this article have been included as part of the supplementary information. Supplementary Table S1 provides the scoring criteria for evaluating the severity of peritoneal adhesions. Supplementary Tables S2-S4 provide the scoring criteria for neovascular granuloma, fibrosis, and inflammation in HE-

View Article Online
DOI: 10.1039/D5NR04935K

stained sections. The Supplementary Figures (Fig S1-S11) mentioned in this paper have also been included in the supplementary information. The original data for EDS-Mapping and SDS PAGE protein bands (raw photographs, grayscale images, and annotations) are available in the supplementary files.

Acknowledgements

This work was supported by Natural Science Foundation of China (82373825), the open fund of State Key Laboratory of Advanced Drug Formulations for Overcoming Delivery Barriers and Qingfeng Scholar fund (Shanghai Medical College, Fudan University). We thank Drs. Y. J. and H. L. for their consultation and assistance regarding the clinical status of the disease and drug selection.

References

1. J. Tang, Z. Xiang, M. T. Bernards and S. Chen, Acta Biomaterialia, 2020, 116, 84-104.
2. E. Zarnescu, N. Zarnescu and R. Costea, Diagnostics, 2021, 11, 2382.
3. M. Ouaïssi, S. Gaujoux, N. Veyrie, E. Denève, C. Brigand, B. Castel, J. J. Duron, A. Rault, K. Slim and D. Nocca, Journal of Visceral Surgery, 2012, 149, e104-e114.
4. N. Tabibian, E. Swehli, A. Boyd, A. Umbreen and J. H. Tabibian, Annals of Medicine and Surgery, 2017, 15, 9-13.
5. W. Ye, Z. Cui, L. Hao, X. Han, S. Ma, L. Duan, Z. Zhou, J. Zhao, K. Hong, L. Sun and R. Jiang, Chemical Engineering Journal, 2025, 517, 164421.
6. L. Pascual-Antón, P. Sandoval, H. Tomero-Sanz, M. Terri, R. Strippoli, Í. García-Sanz, C. Marín-Campos, M. Á. del Pozo, M. Obaid, V. Garcia, P. A. Smith, T. J. Keane, M. M. Stevens and M. López-Cabrera, Science Translational Medicine, 17, eadn3179.
7. R. Aziz, F. Jawed, A. Jain, M. Hussain and S. A. Khan, Journal of Bodywork and Movement Therapies, 2025, 45, 1058-1065.
8. K. Rozita, T. Mahmoud, A. F. Gorgon, F. Leyla, M. Amir Hossein, A. Mohsen and A. Mohammad-Hassan, Current Molecular Pharmacology, 2024, 17, 1-6.
9. Z. Bayhan, S. Zeren, F. E. Kocak, C. Kocak, R. Akcılar, E. Kargı, C. Tiryaki, F. Yaylak and A. Akcılar, Journal of Surgical Research, 2016, 201, 348-355.
10. M. J. Strowitzki, A. S. Ritter, P. Radhakrishnan, J. M. Harnoss, V. M. Opitz, M. Biller, J. Wehrmann, U. Keppler, J. Scheer, M. Wallwiener, T. Schmidt, A. Ulrich and M. Schneider, Scientific Reports, 2017, 7, 13151.
11. R. Gao, F. Li, Y. Zhang, P. Kong, Y. Gao, J. Wang, X. Liu, S. Li, L. Jiang, J. Zhang, C. Zhang, Z. Feng, P. Huang and W. Wang, Biomater Sci, 2023, 11, 6573-6586.
12. T. Zhang, Y. Huang, Y. Gong, X. Shi, D. Xiao, L. Ren, X. Dai, Z. Zeng and C. Zhao, Acta Biomaterialia, 2024, 184, 98-113.
13. Y. Ren, G. Li, E. Li, K. Deng, J. Lian, Q. Gao, H. Wang, X. Wang, Z. Wang, T. Shen, Z. Jiang, X. Li and G. Qiu, European Journal of Pharmacology, 2024, 964, 176272.
14. A. Sivanantham, D. Pattarayan, N. Rajasekar, A. Kannan, L. Loganathan, R. Bethunaickan, S. K. Mahapatra, R. Palanichamy, K. Muthusamy and S. Rajasekaran, Inflammation Research, 2019, 68, 1011-1024.
15. J. Chen, X. An, L. Xu, Y. Gao, M. Zhou and Z. Liu, Small, 2024, 20, e2306598.
16. J. Watanabe, F. Ishida, H. Ishida, Y. Fukunaga, K. Watanabe, M. Naito and M. Watanabe, Surgery Today, 2019, 49, 877-884.
17. Y. Mao, Y. Zeng, Y. Meng, Y. Li and L. Wang, European Polymer Journal, 2022, 178, 111499.
18. Y. Zhao, Z. Huang, F. Wang, Y. Lu, H. Zou, Y. Wang, S. Song and R. Huang, Advanced Materials, 2026, 38, e18217.
19. W. Wang, Y. Ren, Q. Yu, L. Jiang, C. Yu, Z. Yue, Y. Wang, J. Lu, P. Che, J. Li and H. Sun, Materials Today Bio, 2024, 29, 101312.
20. J. Zhang, X. Luo, J. Liu, M. Wu, J. Feng and J. Zhou, Advanced Healthcare Materials, 2025, 14, 2404082.
21. N. Purandare, K. J. Kramer, P. Minchella, S. Ottum, C. Walker, J. Rausch, C. R. Chao, L. I. Grossman, S. Aras and M. A. Recanati, J Clin Med, 2022, 11.
22. J. Vandewalle, A. Luypaert, K. De Bosscher and C. Libert, Trends in Endocrinology & Metabolism, 2018, 29, 42-54.
23. A. A. Sağıroğlu, Y. Özsoy and Ö. Özer, Journal of Drug Delivery Science and Technology, 2020, 58.
24. S. S. Ruppel and J. Liang, Langmuir, 2022, 38, 5020-5029.
25. K. Wang, W. Mao, X. Song, W. Feng, G. Wang, T. Zhang, T. Xu, M. Chen, Y. Chen and B. Peng, Advanced Functional Materials, 2024, 34.
26. C. Jian, Y. Hong, H. Liu, Q. Yang and S. Zhao, International Journal of Pharmaceutics, 2025, 669, 125087.
27. R. Micillo, M. Iacomino, M. Perfetti, L. Panzella, K. Koike, G. D'Errico, M. d'Ischia and A. Napolitano, Pigment Cell Melanoma Res, 2018, 31, 475-483.
28. G. Wei, D. Jiang, S. Hu, Z. Yang, Z. Zhang, W. Li, W. Cai and D. Liu, ACS Applied Materials & Interfaces, 2021, 13, 47341-47353.
29. S. Hu, X. Pei, L. Duan, Z. Zhu, Y. Liu, J. Chen, T. Chen, P. Ji, Q. Wan and J. Wang, Nature Communications, 2021, 12, 1689.
30. Y. Li, Y. Cheng, Y. Wu, Z. Wang, X. Ma, J. Zhao, Z. Yang and Y. Ji, Industrial & Engineering Chemistry Research, 2024, 63, 3140-3151.
31. K. H. S. Sy, L. W. C. Ho, W. C. Y. Lau, H. Ko and C. H. J. Choi, Langmuir, 2018, 34, 14033-14045.
32. V. Ball, D. D. Frari, V. Toniazzo and D. Ruch, Journal of Colloid and Interface Science, 2012, 386, 366-372.
33. F. Bernsmann, B. Frisch, C. Ringwald and V. Ball, Journal of Colloid and Interface Science, 2010, 344, 54-60.
34. N. Uyama, H. Tsutsui, S. Wu, K. Yasuda, E. Hatano, X.-Y. Qin, S. Kojima and J. Fujimoto, Scientific Reports, 2019, 9, 17558.
35. M. Saraiva, P. Vieira and A. O'Garra, Journal of Experimental Medicine, 2019, 217, e20190418.
36. A. G. York, M. H. Skadow, J. Oh, R. Qu, Q. D. Zhou, W.-Y. Hsieh, W. K. Mowel, J. R. Brewer, E. Kaffe, K. J. Williams, Y. Kluger, S. T. Smale, J. M. Crawford, S. J. Bensinger and R. A. Flavell, Nature, 2024, 627, 628-635.
37. C.-T. Chen, F. J. Martin-Martinez, G. S. Jung and M. J. Buehler, Chemical Science, 2017, 8, 1631-1641.
38. I. D. Lima Cavalcanti, F. H. Xavier Junior, N. S. Santos Magalhães and M. C. d. B. Lira Nogueira, International Journal of Pharmaceutics, 2023, 641, 123063.
39. J. Liu, L. Shi, X. Lu, C. Zhou, Z. Zhou, Q. Lv, L. Wang and Z. Wang, Chemical Engineering Journal, 2024, 485, 150001.
40. G. Wei, X. Chen, G. Wang, P. Jia, Q. Xu, G. Ping, K. Wang and X. Li, Drug Des Devel Ther, 2015, 9, 3083-3098.
41. J. Lim, S. Zhang, J.-M. Heo, M. C. Dickwella Widanage, A. Ramamoorthy and J. Kim, ACS Applied Materials & Interfaces, 2024, 16, 31864-31872.
42. M. P. Murphy, H. Bayir, V. Belousov, C. J. Chang, K. J. A. Davies, M. J. Davies, T. P. Dick, T. Finkel, H. J. Forman, Y. Janssen-Heininger, D. Gems, V. E. Kagan, B. Kalyanaraman, N.-G. Larsson, G. L. Milne, T. Nyström, H. E. Poulsen, R. Radi, H. Van Remmen, P. T. Schumacker, P. J. Thornalley, S. Toyokuni, C. C. Winterbourn, H. Yin and B. Halliwell, Nature Metabolism, 2022, 4, 651-662.
43. L.-K. Yang, L. B. Sy, J.-F. Liu, T.-M. Chang, J.-F. Lin and C.-J. Chang, Journal of Pharmacological Sciences, 2025, 159, 292-300.
44. K. Hara, C. Hamada, K. Wakabayashi, R. Kanda, K. Kaneko, S. Horikoshi, Y. Tomino and Y. Suzuki, PLOS ONE, 2017, 12, e0184332.
45. J. Liu, L. Shi, Y. Wang, M. Li, C. Zhou, L. Zhang, C. Yao, Y. Yuan, D. Fu, Y. Deng, M. Liu, G. Wang, L. Wang and Z. Wang, Nano Today, 2022, 47, 101627.
46. G. M. Saed, H. M. Abu-Soud and M. P. Diamond, Fertility and Sterility, 2004, 82, 1198-1205.
47. C. Liu, W. Yao, M. Tian, J. Wei, Q. Song and W. Qiao, Biomaterials, 2018, 179, 83-95.
48. M. Zhou, X. An, Z. Liu and J. Chen, ACS Biomaterials Science & Engineering, 2024, 10, 1031-1039.
49. L. Yan, J. Wang, X. Cai, Y.-C. Liou, H.-M. Shen, J. Hao, C. Huang, G. Luo and W. He, MedComm, 2024, 5, e658.
50. B. Zhang, Q. Li, Q. Xu, B. Li, H. Dong and Y. Mou, International Journal of Nanomedicine, 2023, 18, 4601-4616.
51. C. Li, C. Deng, S. Wang, X. Dong, B. Dai, W. Guo, Q. Guo, Y. Feng, H. Xu, X. Song and L. Cao, Redox Biology, 2024, 70, 103059
52. X. Bao, J. Zhao, J. Sun, M. Hu and X. Yang, ACS Nano, 2018, 12, 8882-8892.
53. T. Joo, K. Sowndhararajan, S. Hong, J. Lee, S.-Y. Park, S. Kim and J.-W. Jhoo, Saudi Journal of Biological Sciences, 2014, 21, 427-435.
54 A. ShaykhoIslami, M. Ghasemian, M. Zardast and M. Farzad, Annals of Medicine and Surgery, 2021, 71, 102928.

View Article Online
DOI: 10.1039/D5NR04935K

Data Availability Statement:

The data supporting this article have been included as part of the supplementary information. Supplementary Table S1 provides the scoring criteria for evaluating the severity of peritoneal adhesions. Supplementary Tables S2-S4 provide the scoring criteria for neovascular granuloma, fibrosis, and inflammation in HE-stained sections. The Supplementary Figures (Fig S1-S11) mentioned in this paper have also been included in the supplementary information. The original data for EDS-Mapping and SDS PAGE protein bands (raw photographs, grayscale images, and annotations) are available in the supplementary files.